J Mar Sci Technol (2005) 10:159–172
DOI 10.1007/s00773-005-0201-6

Journal of
Marine Science
and Technology

Original articles

Propeller wake analysis in nonuniform inflow by LDV phase sampling techniques

Mario Felli and Fabio Di Felice

INSEAN (Italian Institute for Naval Architecture Studies and Testing), Via di Vallerano 139, 00137, Rome, Italy

Abstract A laser Doppler velocimetry (LDV) phase sampling technique is developed and adopted for the analysis of the flow upstream and behind a four-blade, highly skewed installed propeller in the case of a twin-screw ship model in a large circulating water channel. The technique implemented allows the reconstruction of the 3D flow field as a function of propeller angle in transversal planes located as close as possible to the blade trailing and leading edges. The main features of the propeller installation are highlighted, as well as the strong and complex interaction of the propeller with the hull wake, especially in the brackets region. The high level of detail and accuracy of the data acquired would be a powerful tool for the development and validation of computational codes applied to this topic.

Key words Propeller wake · Laser Doppler velocimetry (LDV) · Phase sampling · Nonuniform inflow

List of symbols

ν	kinematic viscosity
λ	scale ratio
ε	slot semiamplitude
ϑ	reference blade angular position
Γ	blade bound circulation
$\Delta\alpha$	angle of attack variation
ω_x	vorticiy along the x-axis
A_0	propeller disc area (πR^2)
A_p	propeller expanded area
$c_{0.7}$	blade chord at $0.7R$
D, R	propeller tip diameter and radius
I	blade load index
J	advance coefficient ($U_\infty/(nD)$
KE	free stream kinetic energy
n	propeller rotation speed
P	propeller pitch
r	local propeller radius
R_m	measurement grid external radius
TKE	turbulent kinetic energy
U_∞	free stream velocity
V_{ax}, V_{tan}	axial and tangential velocity
V_x, V_y, V_z	velocity components in the propeller reference frame
X_g, Y_g	axial velocity centroid coordinates
Z	propeller blade number

Address correspondence to: M. Felli (m.felli@insean.it)
Received: July 2, 2004 / Accepted: June 7, 2005

1 Introduction

The accurate experimental investigation and assessment of the wake of an installed propeller play a fundamental role in the naval field where propeller performances are largely dependent on the upstream wake. Nonuniform inflow induces variable radial and angular fluid dynamic loads along the blade, and hence a thrust and torque distribution which changes during the revolutions. These changes lead to propeller-induced vessel vibrations, unsteady cavitation, and noise generation. The increased complexity of propeller blade geometry due to demanding requirements for reduced noise levels and lower propeller-induced structural vibrations, expecially for cruise ships, enhances interest in detailed measurements of the propeller flow field. Such measurements are useful to check conformity with the design requirements, for instance by using the deduced blade section drag coefficients and bound circulation distribution, as in Kobayashi[1] and Jessup,[2] as well as to acquire information for completely new designs. Furthermore, the experimental investigation provides baselines to develop, improve, and integrate theoretical computations. The development of non-intrusive techniques, such as laser Doppler velocimetry (LDV) and particle image velocimetry (PIV), allows suitable experimental investigations of complex fluid dynamic fields, such as propeller wakes, where the occurrence of strong vortical structures, turbulent fluctuations

(George and Lumley[3]), three-dimensional boundary layers, and marked velocity gradients[1,4,5] puts very strict requirements on the choice of measurements techniques.

In particular, LDV is an effective tool for this kind of analysis because it allows, in addition to a high accuracy and resolution of the measurements, a better optical access compared with a multipoint technique such PIV. A typical example is for surveys of propeller inflow, where the occurrence of propeller, shaft, hull, and appendages makes optical access too complex.

Many reports on the behavior of a propeller in uniform inflow can be found in literature. The 3D flow field in a transverse plane behind a propeller can easily be reconstructed by sweeping the measured volumes of a three-component velocimetry system along a radius[6] or along two orthogonal radial directions of a two-component velocimetry system.[2,7–9] By using the same procedure and hot-wire anemometry, Hyun and Patel[10] extended the study of propeller flow to the case of an axisymmetric inflow (propeller installed in the wake of an axisymmetric body).

An experimental survey of a real propeller installation is more complex. In such a case, the axisymmetry hypothesis is no longer valid, and an experimental investigation of the propeller wake requires a complete and sufficiently dense grid in the investigation plane, for a given propeller angle, in order to resolve the flow structure during propeller revolutions.

Therefore, the phase sampling techniques developed for the analysis of a 3D propeller wake in a uniform incoming flow have to be extended to the whole propeller plane, and no longer to one or two radial lines only. For these reasons, the experimental analysis is particularly onerous, and requires a long time and considerable power. This explains the lack of available data in the literature regarding flow-field surveys in phase around installed propellers. The published literature for experimental investigations of a propeller wake in nonuniform inflow are restricted to one article by Rood and Anthony,[11] which studies the flow interactions for a combined propeller–hull–appendage on an axisymmetric body by means of LDV. However, in this study, measurements were made only along a normal plane upstream of the propeller disc, inside a sector of a circle of 90° in the upper left quadrant of the annular flow, as viewed upstream.

In the present case, the study of the flow field of an installed propeller was carried out by measuring the three velocity components along two transverse sections of the wake, up and downstream of the propeller disc, and in phase with the propeller's position. The aim of this work was to provide a high level of detail and accuracy that would represent a powerful tool for the analysis of complex phenomena, and for the development and validation of computational codes applied to such a flow. For this reason, all the geometry and the experimental results are available for free downloading at http://crm.insean.it.

Although the wake details are strictly dependent on the geometry of the propeller, the inflow characteristics, and the loading conditions, the results of this investigation will be discussed with an emphasis on those flow features that characterize an inward rotating propeller installation.

2 Experimental setup

The measurements were conducted in the INSEAN circulating water channel. This is a free surface cavitation channel with a test section which is 10 m long by 3.6 m wide by 2.25 m deep. The maximum velocity that can be achieved in this test section is 5.2 m/s. The pressure in the test section can be reduced to a minimum of 30 mbar.

A propeller installation was simulated by using the starboard half of a twin-screw vessel of 6.4 m in length. The propeller and the aft region between the transom and the frame n. 8 were scaled by a factor $\lambda = 20$. The fore region was contracted in the longitudinal direction in order to fit into the channel test section while preserving the sectional area distribution (Fig. 1). This configuration was a trade off between the exigencies of needing to increase the scale of the model in order to work with a larger Reynolds number, and thus to be better able to reproduce the propeller flow field of the full-scale ship (i.e., reduce the laminarity effects on the propeller blades), and to fit into the channel test section. The solution of the starboard half of the model allowed us to move the measurement region away from the facility wall, and hence to minimize the effects of reflected waves.

The four-blade, adjustable-pitch, highly skewed propeller (Table 1) was installed on an open shaft supported by two bearings that were attached to the hull by shaft brackets with an "L" configuration, as shown in Fig. 2. The brackets were trimmed and counter rotating with respect to the propeller at 7° from the centerplane (vertical bracket) and the undisturbed water surface (horizontal bracket).

A sketch of the experimental set-up is shown in Fig. 3. Flow velocity was measured by means of a two-component back-scatter LDV system, which consists of a 5-W argon laser, a 2-component underwater fiber optic probe, a 40-MHz Bragg cell for the velocity versus ambiguity removal, and two TSI IFA 550 Doppler processors. The three-dimensional velocity field measurements were performed in two separate steps by means of two different optical configurations, measuring the

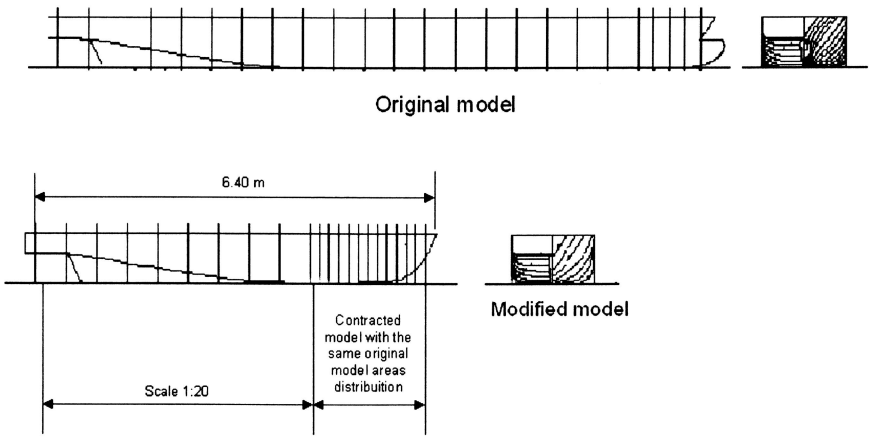

Fig. 1. Sketch of the model hull

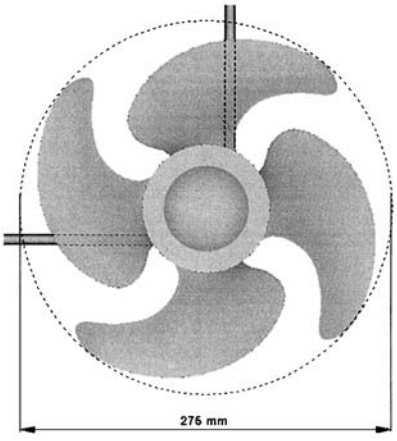

Fig. 2. "L" brackets configuration (looking upstream)

Table 1. Features of the propeller model

Blade number, n	4
Scale ratio, λ	20
Diameter, D_p	275 mm
Pitch–diameter ratio, P/D_{07}	1.636
Expanded area–disc area ratio, A_p/A_0	0.703

components on a vertical plane parallel (V_x, V_z) and perpendicular (V_y, V_z) to the rotating shaft (Fig. 4).

A rotary 3600-pulse/revolution encoder supplied the propeller position with an angular accuracy of 0.1°. The encoder signals were processed by a synchroniser which provided the angular position of the propeller to a two-bytes digital port available on the LDV master processor. The underwater probe was set up on a computer-controlled traversing system which allows a displacement accuracy of 0.01 mm in all directions, and achieves a highly automated LDV system. Particular care was required in the initial location of the volume measurement in order to reduce positioning errors in the two optical configurations. This was carried out by aligning the volume measurements on a special target with a known position with respect to the center of the propeller disc.

In order to improve the Doppler signal processor data rate and to reduce the acquisition time at each point, the water in the tunnel was seeded with 1 μm titanium dioxide (TiO_2) particles. Seed injection was done using a special rake device consisting of many small pipes with a large number of tiny holes, placed 1 m upstream of the model ship. The adoption of this device ensured a homogeneous distribution of the tracers without significantly disturbing the flow. Water seeding was performed at the start of the tests because it was found that the density of the seed particles remains almost constant for a long time in the facility.

Data acquisition was accomplished by using a low-end personal computer, while the postprocessing analysis, requiring several Gbytes of data storage and computational resources, was performed on a workstation.

3 Measurement grid and test conditions

The tests were carried out at a propeller angular velocity $n = 7.7$ r.p.s. and a tunnel water velocity $U_\infty = 2.4$ m/s, which corresponds to an advance ratio $J = U_\infty/(nD)$ of 1.1 and a blade Reynolds number at 0.7 r/R Re = $(c_{0.7}U_{0.7}/\nu)$, where $c_{0.7}$ is the chord length at 0.7R, and $U_{0.7}$ is the undisturbed total velocity at 0.7R, i.e., of $3.7 \cdot 10^5$. The speed of the facility was set to be a compromise between the opposite exigency of increasing the Reynolds number and preventing waves growing so that they would interfer with the test conditions.

Measurements were performed along two transverse planes of the wake located upstream ($x/R = -0.49$) and

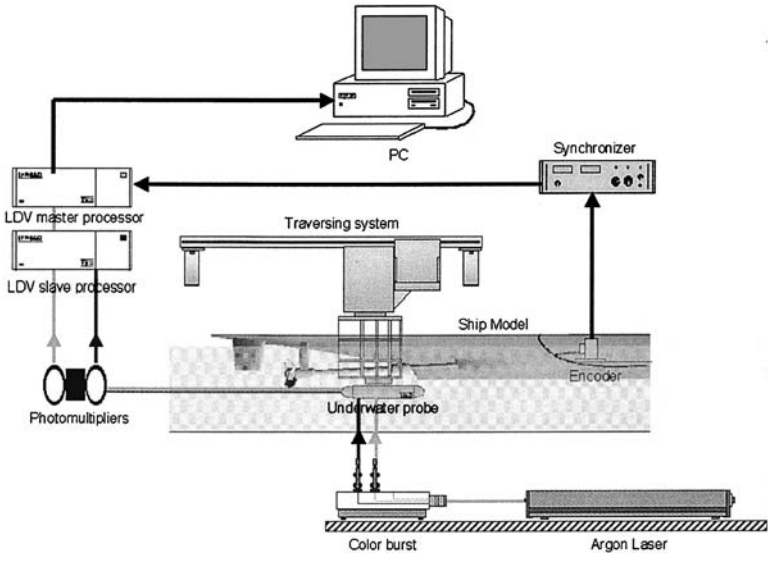

Fig. 3. Sketch of the experimental setup

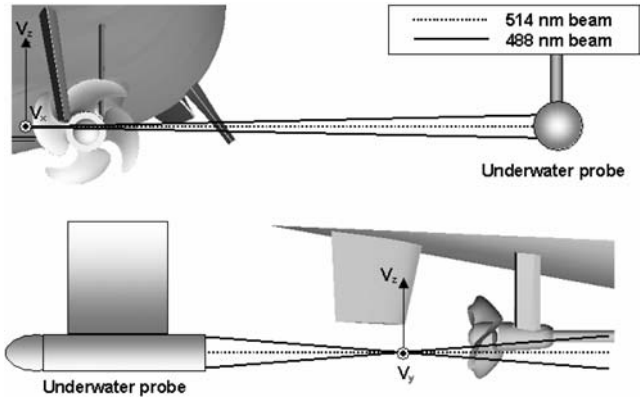

Fig. 4. Laser–Doppler velocimetry (LDV) optical configurations

downstream ($x/R = 0.742$) of the propeller disc (Fig. 5). The upstream plane was $0.14R$ downstream of the trailing edge of the shaft brackets. The location of the measurement planes was as close as possible to the propeller disc, allowing optical access to the whole measurement plane. A third measurement plane corresponding to the propeller disc was adopted for the nominal wake survey.

The measurement grid was defined as a compromise solution between ensuring good spatial resolution and minimizing the number of points. For this purpose, a z and y uniform Cartesian map, which was denser around the brackets, was used (Fig. 5). This was to ensure the good spatial resolution which is necessary to resolve the wake structures of the propeller, especially where the highest velocity gradients are expected, and to reduce the time required for the tests.

The measurement grid size (external radius R_m = 158.125 mm) was slightly bigger than the propeller radius (R = 137.5 mm) is order to resolve the blade tip structures, any possible ship boundary layer trace, and the wake variations along the diameter. In order to cover the complete disc area of the propeller, two grids of about 400 points ($\Delta y = \Delta z \cong 12$ mm) were adopted, in a Cartesian system with the origin at the center of the propeller disc, the x axis coincident with the shaft axes, fore–aft oriented, the y axis horizontal, starboard oriented, and the z axis vertical, upward oriented.

4 Phase sampling technique

The correspondence between the randomly acquired velocity bursts and the propeller's angular position was carried out using phase sampling techniques. The procedure adopted was the tracking triggering technique (TTT) described by Stella et al.,[9] because it allows the acquisition process to be fast and efficient. Samples velocities are acquired when a Doppler signal is detected in any of the two LDV channels, and these are tagged with the angular position of the reference blade at the time of measurement. This process is repeated independently in the two LDV channels because it was found that Doppler burst detection is a random event and not necessary simultaneous in both channels.

During postprocessing, data are ordered inside angular slots of constant width, and a statistical computation is performed for each slot in order to obtain the mean flow field and turbulence intensity information. The choice of the slotting parameter is critical for this kind

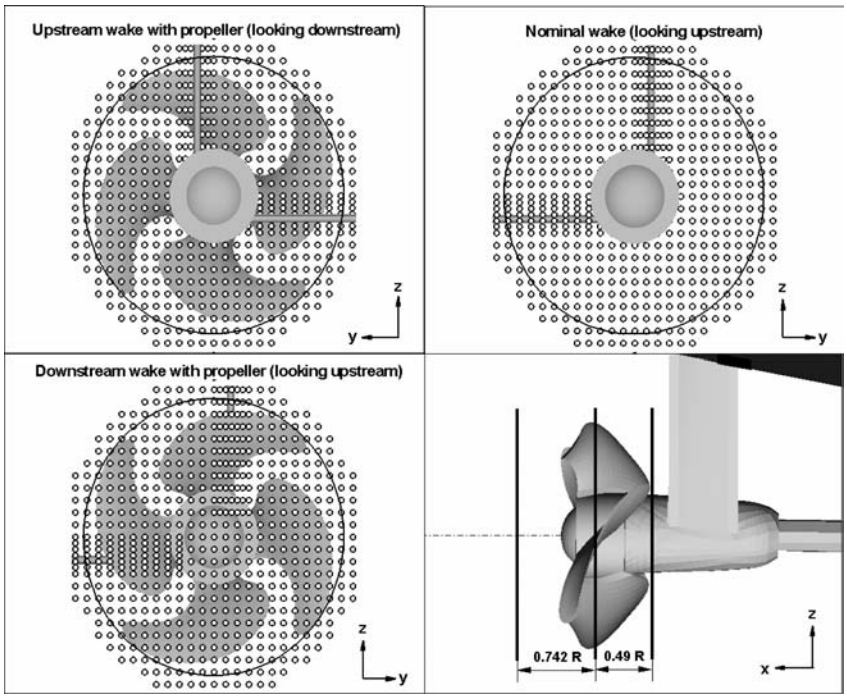

Fig. 5. Measurement grids

of analysis. In fact, a compromise should be adopted between the need to increase the angular resolution in order to capture the velocity gradients (smaller slots), and the need to have an adequate number of samples inside the slot for consistency in the statistical estimators (larger slots). For these reasons, the standard slotting procedure (N contiguous slots, 2ε wide, from 0° to 360°) provides poor statistical processing accuracy. Hence, more complex slotting procedures had to be implemented in order to obtain an optimal compromise between statistical requirements and angular resolution, as well as in critical data-rate conditions.

For this purpose, three independent slotting procedures were developed: overlapping, blade slotting, and weighted slotting.[12] The overlapping procedure provides partial overlapping, $\Delta\varepsilon$ wide, for contiguous slots. Therefore, any sample in the overlapping area increases the statistical population in the two overlapped slots simultaneously, with statistical processing advantages. The blade-slotting procedure is based on the hypothesis of considering the propeller blades to be identical in both mechanical and geometric terms. By this hypothesis, the velocity field at any measurement point is a periodic function of time with blade frequency (Fig. 6). Thus, the slotting procedure can be limited inside an angular sector $2\pi/Z$ wide, where Z is the number of blades. A given slot with a center in the angular position θ_i and 2ε wide ($\theta_i - \varepsilon \le \theta(t^*) \le \theta_i + \varepsilon$) will contain all the velocity samples acquired when the angular position is $\theta(t^*) + 2\pi n/Z$ ($n = 0, 1, \ldots, N_{\text{rev}}1$) (Fig. 7). Hence, the

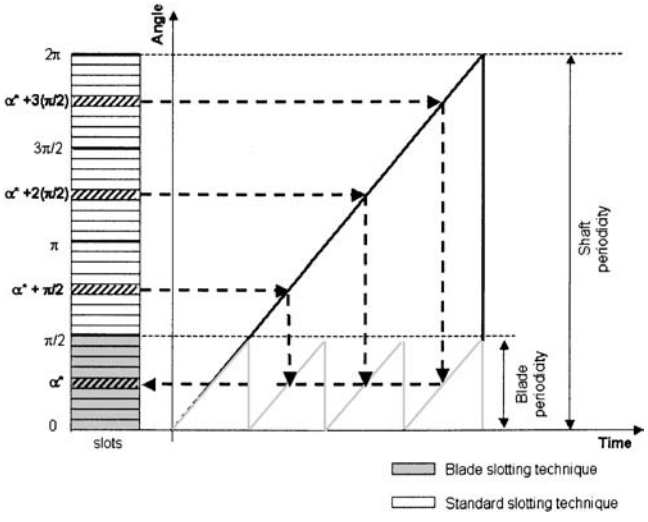

Fig. 6. Blade-slotting procedure for a 4-bladed propeller: all the samples acquired when the reference blade position is $\alpha^* + n \cdot (\pi/2)$ ($n = 1, 2, 3, 4$) pass through the same slot α^* if we consider the blade periodicity (*dashed line*)

sample population of each slot is increased by a factor corresponding approximately to the number of propeller blades.

In the weighted slotting procedure, a weighted average is introduced into the statistical analysis so that the influence of each sample will progressively decrease under a fixed law (linear, Gaussian) with its distance

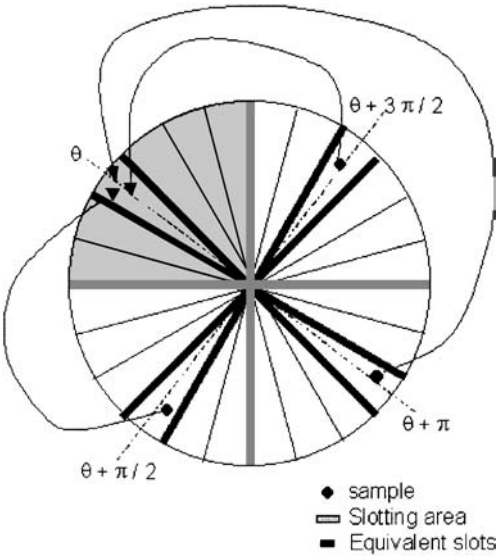

Fig. 7. Blade-slotting procedure for a 4-bladed propeller

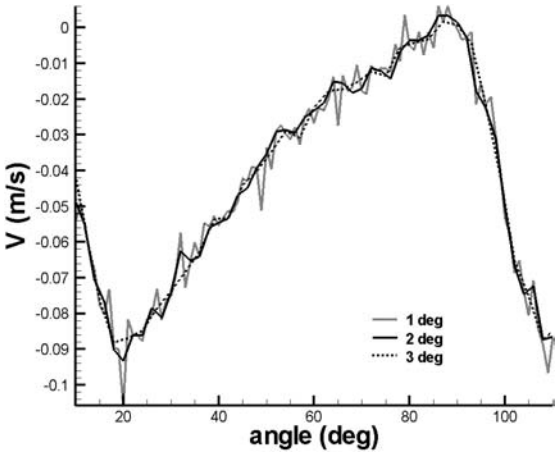

Fig. 8. Slotting technique: effect of slot size

from the slotting center, with an improvement in accuracy.

In this analysis, a statistical evaluation was performed using a blade-slotting technique with 360 overlapping slots, $2\varepsilon = 2°$ wide, and weighted averaging by Gaussian law. In this way, an average of 150–200 samples per slot (obtained at one point within 180 s and at a data-rate of about 200 samples per second) were collected. In addition, the angular resolution is adequate to describe flow regions with high gradients.

5 Measurement uncertainty

Error sources can be divided into three different classes: instrumental accuracy errors, positioning errors, and postprocessing errors.

5.1 Instrumental accuracy errors

In the optical configuration adopted (465 mm focal length in water), the accuracy of the INSEAN LDV system is estimated to be around 1%. A measurement volume transit-time weighting was used to correct for velocity bias. Over the whole measurement area, the influence of the probe and its support, calculated by a potential code, was one order of magnitude less than the accuracy of the measurement technique.

5.2 Positioning errors

LDV probe displacements were carried out by a traversing system with an accuracy of 0.01 mm. A position error within 0.5 mm is made in the LDV probe alignment on the target setting the origin of the coordinate system. The setting of the blade at the angular reference position "zero", performed by using a strobe light triggered by a synchronizer in order to align the blade with a plumb line which crosses the center of the propeller, is estimated to be accurate to within 2°.

5.3 Processing errors

The processing errors are mainly due to the slotting technique during the statistical analysis of the acquired data. The average reading inside each slot smoothes the velocity gradients along the azimuth as a low-pass filter (Fig. 8). However, this effect was found to be negligible for values of the slot width up to 2°.[9] The adoption of a weighted slotting technique can improve the result and reduce this effect.

The uncertainty of the statistical analysis can be assessed by evaluating the confidence interval of the statistical estimators. The statistical population of the velocity samples changes over a wide range (100–400) depending on the fluid dynamic features of the wake. By using Student's t distribution (for which the confidence interval is $\pm t_{0.975}(N)$*rms$/\sqrt{(N-1)}$, with $t_{0.975}(N)$ being Student's t value corresponding to a confidence level of $\alpha = 97.5\%$ and a sample size N), it is possible to estimate the uncertainty of a velocity component to be in the range between about 0.2% and 2.4% of the measured mean velocity. The maximum values of the confidence intervals are achieved in the tip vortex, where only 100 samples, on average, are available to compute statistics owing to the strong centrifugal forces which locally reduce the probability of having useful particles.[14]

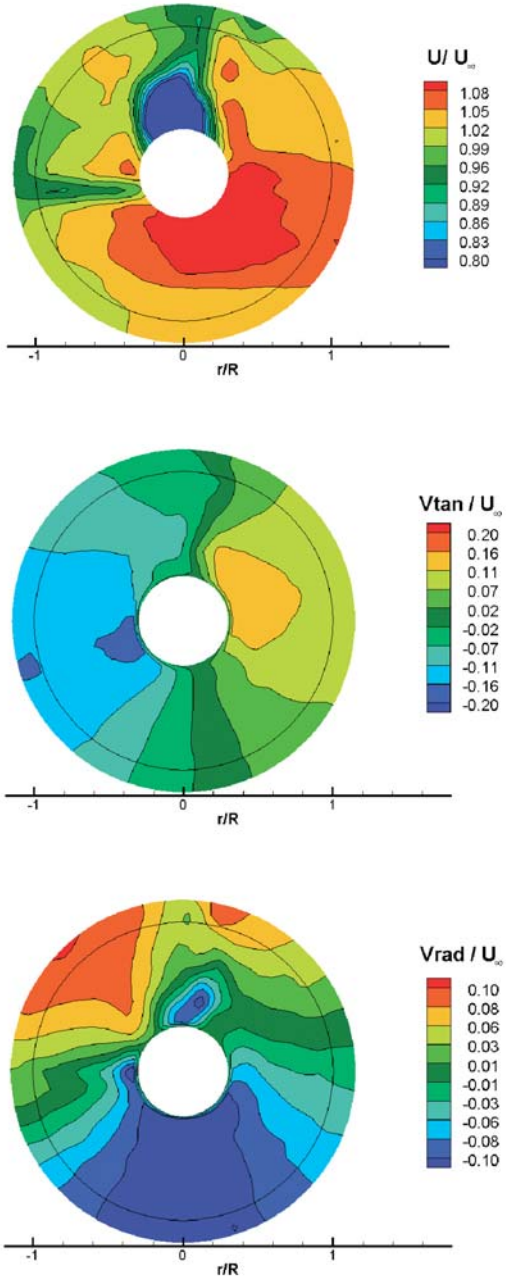

Fig. 9. 3D wake in the propeller plane with no propeller is nondimensional by the free-stream velocity. The iso-contours describe the behavior of the axial (*top*), tangential (*center*), and radial (*bottom*) components

6 Wake analysis

6.1 Nominal wake

Before considering the details of the propeller wake, and to have a better understanding of the behaviour of the flow field during propeller rotation, the mean field results at $x/R = 0$, measured without the propeller, are discussed. This approach is particularly useful because it allows as to point out the contribution to the flow

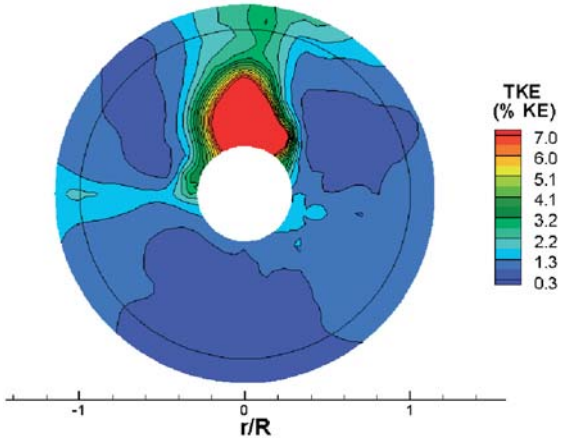

Fig. 10. Turbulent wake (TKE as a percentage of the free-stream kinetic energy) in the propeller plane with no propeller

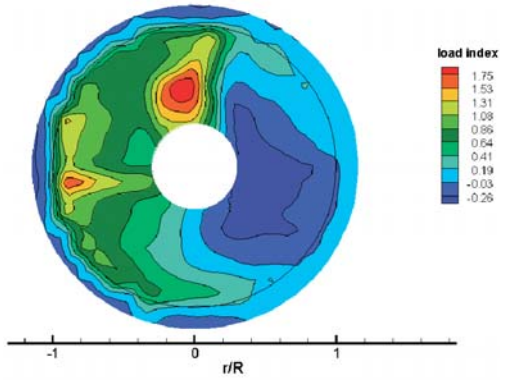

Fig. 11. Hydrodynamic load index distribution in the propeller plane

perturbation induced by the hull and locally by its appendages.

The velocity distribution shows behavior typical of that for twin-screw ships with "L"-bracket configuration, and the following characteristics should be noted.

— The main influence on the flow near the propeller is the potential flow effect of the hull. The influence of the hull boundary layer on the flow here is secondary, even if it can influence the outer regions of the propeller disc near the ship wall. For this reason, the wake coefficient (U/U_∞), calculated averaging the axial component of the nominal wake over the area investigated (Fig. 9, top), is around 0.95, which is a typical value for twin-screw ships.
— The cross flow is generally directed upward and toward the hull center-plane owing to the shape of the hull in the stern sections (Fig. 9, center and bottom).
— The wakes of the brackets and the shaft are clearly apparent in the axial velocity as well as in the distribution of the turbulence levels (Fig. 10). A separate

region in the junction of the vertical brackets with the shaft can be seen.

— The effect of the brackets is important because a strong deformation of the wake is locally induced. They act as wings, causing a momentum transfer from the axial to the transverse components. The wide turbulent region which is recognizable behind the vertical bracket can be ascribed both to the shaft wake, directed upward as a consequence of the stern shape, and to the appendage hydrodynamic incidence. The angle of attack of the appendage is very close to its critical value, and hence causes the release of a thick wake, clearly apparent in the isocontours in Fig. 10.

The effect of the nominal wake on the propeller performance can be estimated by introducing a blade hydrodynamic load index. This parameter is defined as

$$\mathrm{BL}(\vartheta)=\frac{\int_{c1(y,z,\vartheta)}^{c2(y,z,\vartheta)} I(r,\vartheta)\cdot \mathrm{d}c}{\int_{c1(y,z,\vartheta)}^{c2(y,z,\vartheta)} \mathrm{d}c} \tag{1}$$

where

— $I(y, z)$ is the local load index (Fig. 11) estimated by considering the dynamic pressure on the blade and the lift coefficient proportional to the incidence variation $\Delta\alpha(y, z)$:

$$I(r,\vartheta)=\frac{1}{2}\frac{\left[\left(V_{\mathrm{ax}}^2(r,\vartheta)+(\overline{\omega}\cdot r)+V_{\tan}(r,\vartheta)\right)^2\right]\cdot\Delta\alpha(r,\vartheta)}{U_\infty^2} \tag{2}$$

— $\Delta\alpha(y, z)$ is the incidence variation with respect to the case of a propeller operating in uniform inflow:

$$\Delta\alpha(r,\vartheta)=\tan^{-1}\left(\frac{\omega\cdot r+v_{\tan}(r,\vartheta)}{V_{\mathrm{ax}}(r,\vartheta)}\right) \tag{3}$$

— $c = c(y, z, \vartheta)$ is the trace of the leading edge of the blade at the angular position ϑ.

The distribution of the blade load index, calculated from the nominal wake on the basis of blade-element theory, is an estimate of the effective loading conditions, neglecting all effects due to the propeller installation (inflow acceleration due to the suction effect, velocities induced by the shed tip vortices, etc.) and the hydrodynamic unsteadiness. The angular evolution of the blade load shows larger values on the port side ($52 < \vartheta < 108$), where the inflow, directed upward, is counter-rotating with respect to the propeller (Fig. 12).

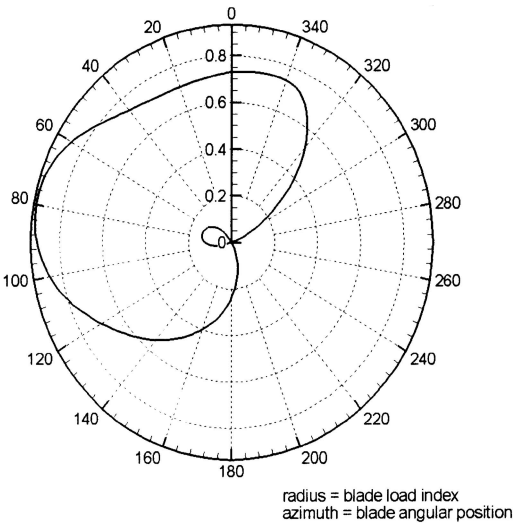

Fig. 12. Hydrodynamic load evolution of the Blade

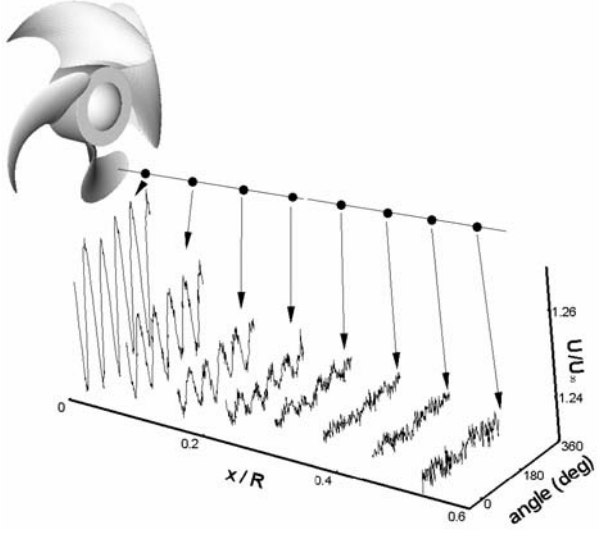

Fig. 13. Propeller influence on the upstream flow from $x/R = -0.44$ to $x/R = -0.96$

6.2 *Phase sampling analysis*

Phase sampling analysis was performed along two transverse planes of the wake: an upstream plane at $x/R = -0.49$ and a downstream plane at $x/R = 0.742$. In particular, the position of the upstream plane is in a region where the induced velocities are already strong, as shown in Fig. 13. Further upstream, these induced velocities tend to disappear quickly. From $x/R = -0.68$, the influence of the propeller can be considered to the negligible.

The angular evolution of the wake is described by the representation of the velocity field during the revolu-

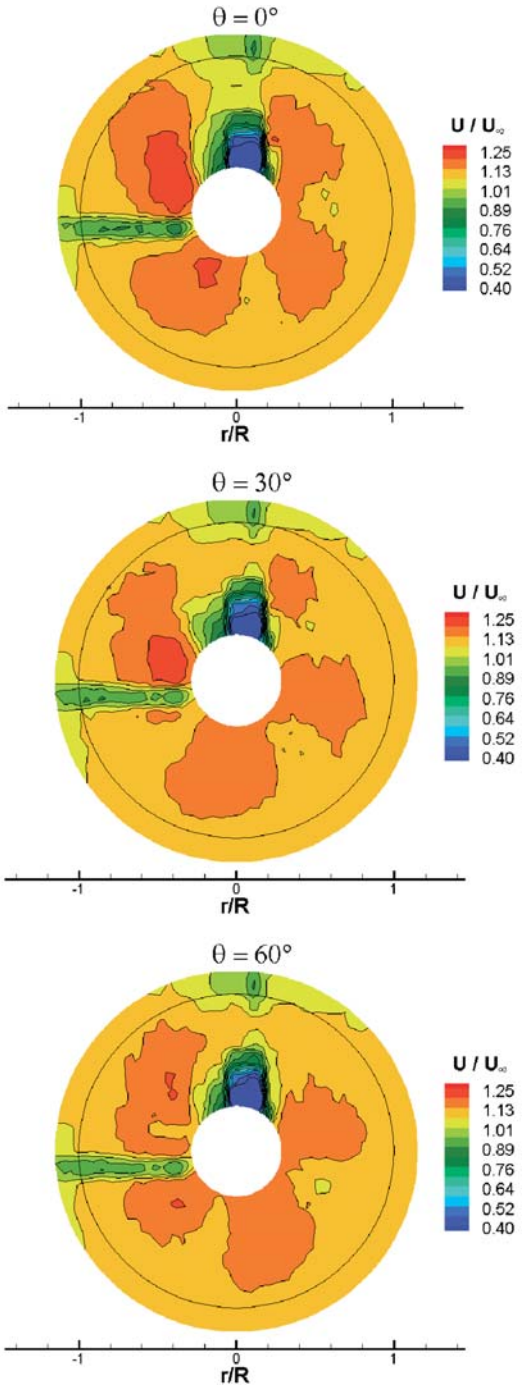

Fig. 14. Upstream wake (x/R = –0.49) with the propeller installed. The axial velocity field is nondimensional by the free stream velocity at 0°, 30°, and 60°

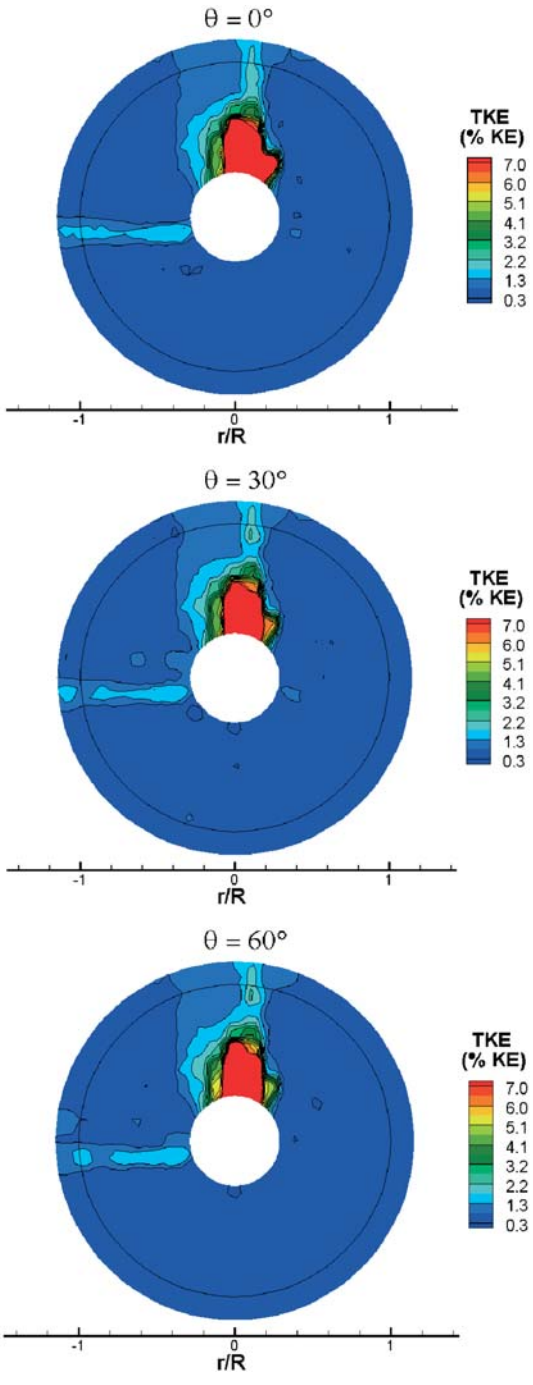

Fig. 15. Upstream wake (x/R = –0.49) with the propeller installed. TKE as a percentage of the free-stream kinetic energy at 0°, 30°, and 60°

tion period. Each velocity distribution in the measurement plane is related to the corresponding angular position of the blade between 0° and 90° (blade slotting procedure):

$$\vec{V}(x,y,z) = F(\theta(t)) \tag{4}$$

where $\theta(t)$ is the angular position of the propeller. For space reasons, only a few representative angular positions of the inward rotating propeller can be shown. Full animations can be downloaded from http://crm.insean.it. The plots show the flow field of the right-hand propeller, rotating in a counterclockwise direction, seen from a downstream viewpoint.

6.3 *Propeller inflow*

The main characteristics of the nominal wake can be recognized in the isocontours representing the mean and turbulent flow fields of the upstream propeller plane (Figs. 14 and 15). The velocity defects of the shaft and the brackets, already pointed out in the nominal wake results, are not removed by the propeller action. The effect of propeller suction is apparent as a four-lobe structure, representing the velocity peaks induced by the blades, which rotate in phase with the propeller blades (Fig. 14). The turbulent field appears very similar to the nominal wake field, with a weak dependence on the propeller phase (Fig. 15). The propeller-induced acceleration leads to a narrower trace of the wakes of the brackets and the shaft and a global reduction in turbulence levels: the former due to the higher Reynolds number of the brackets and the shaft flow, the latter to the negative gradient of the static pressure in the flow direction[15] (Fig. 16).

6.4 *Propeller downstream wake*

Figure 18 shows the evolution of the longitudinal component V_x for the propeller angles $\theta = 0°$, 30°, and 60°, corresponding to one blade passage.

The downstream wake no longer has the axisymmetrical morphology typical of a propeller wake in uniform inflow, and presents the maximum of the induced velocities in the inner and lower parts of the measurement plane, where the hydrodynamic loads of the blade are bigger than elsewhere.

A confirmation of the influence of the hydrodynamic load on the propeller-induced velocity field is given in Fig. 17. This figure shows the angular evolution of the axial velocity as acquired from three different azimuthal positions of the measurement plane at $r = 0.85R$. As expected, the amplitude of the velocity peaks increases where the hydrodynamic load is larger (see Fig. 12).

The velocity defects in the wake of the blades, which are due to the boundary layer shed from the trailing edge and are shown in many isolated propeller analyses,[7,13] are not visible in the measurement plane. This is a consequence of the diffusion and dissipation processes which have already taken place before $x/R = 0.742$, thus fading and smoothing most of the velocity gradients. Furthermore, the low spatial resolution of the measurements with respect to the wake thickness, which is a consequence of the mesh size, plays a role.

The distribution of the downstream wake does not contain any information which resembles the mean axial component of the upstream plane, thus pointing out the capability of the highly skewed, propeller to compensate for and mediate the nonuniformity of the upstream flow. However, this is not true for the stan-

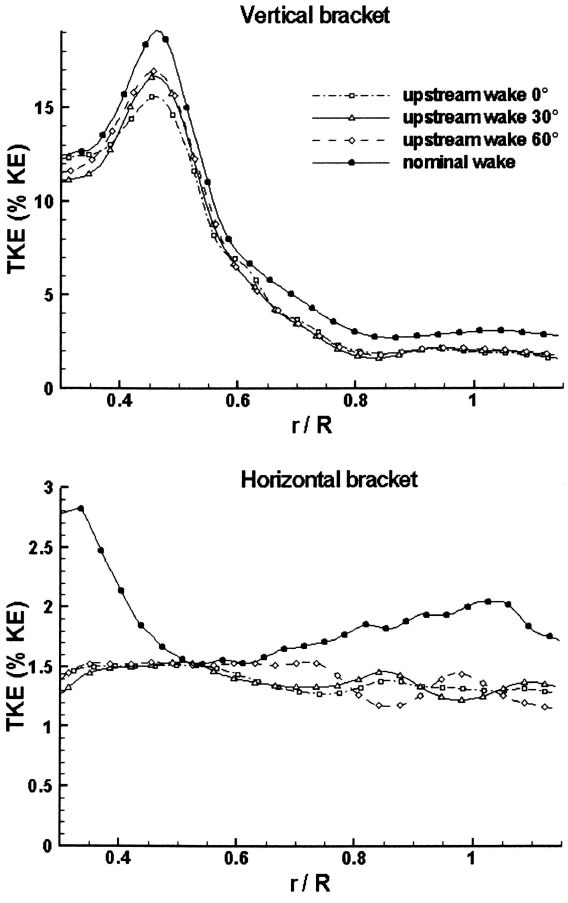

Fig. 16. Radial distribution of the TKE levels (as a percentage of the free-stream kinetic energy) behind the vertical (*top*) and horizontal (*bottom*) brackets

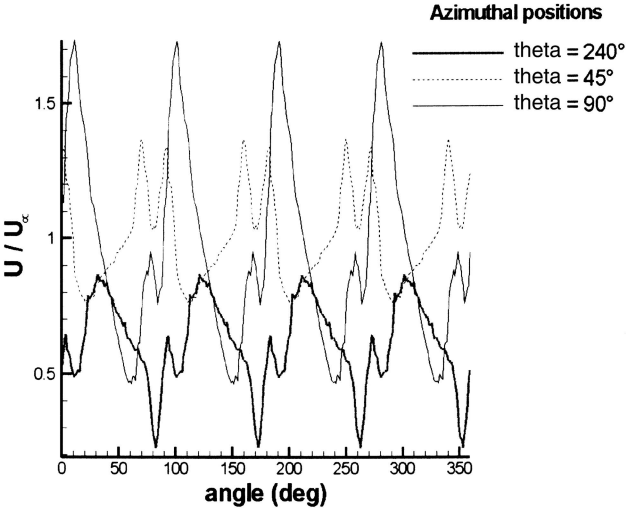

Fig. 17. Angular evolution of the axial velocity at three points on the measurement grid at $r = 0.85R$

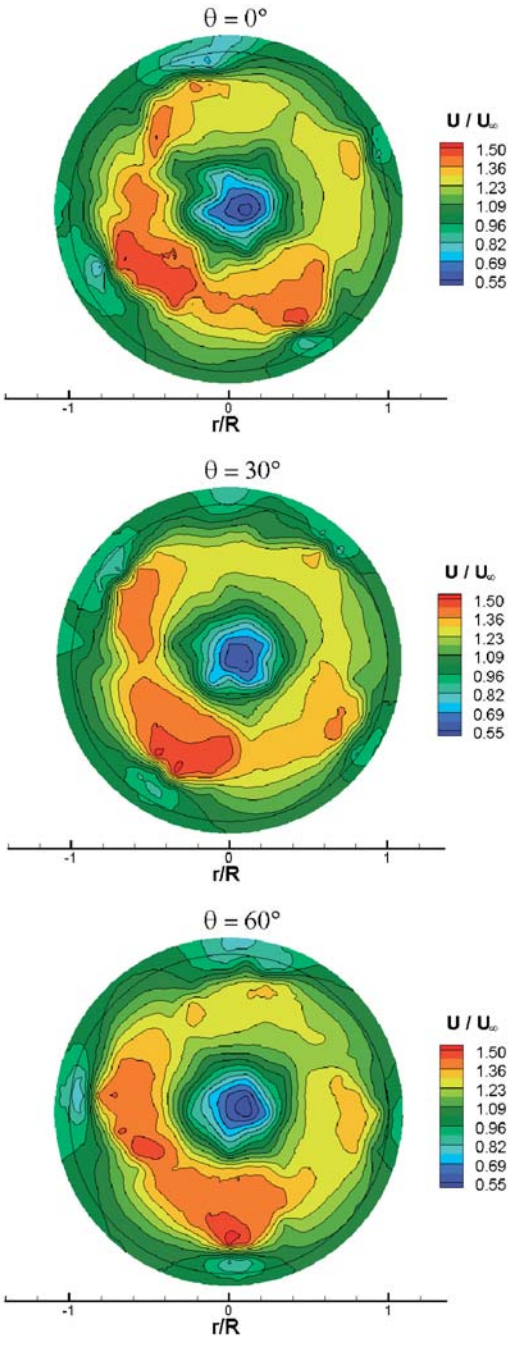

Fig. 18. Downstream wake (x/R = 0.742) with the propeller installed. The axial velocity field is nondimensional by the free-stream velocity at 0°, 30°, and 60°

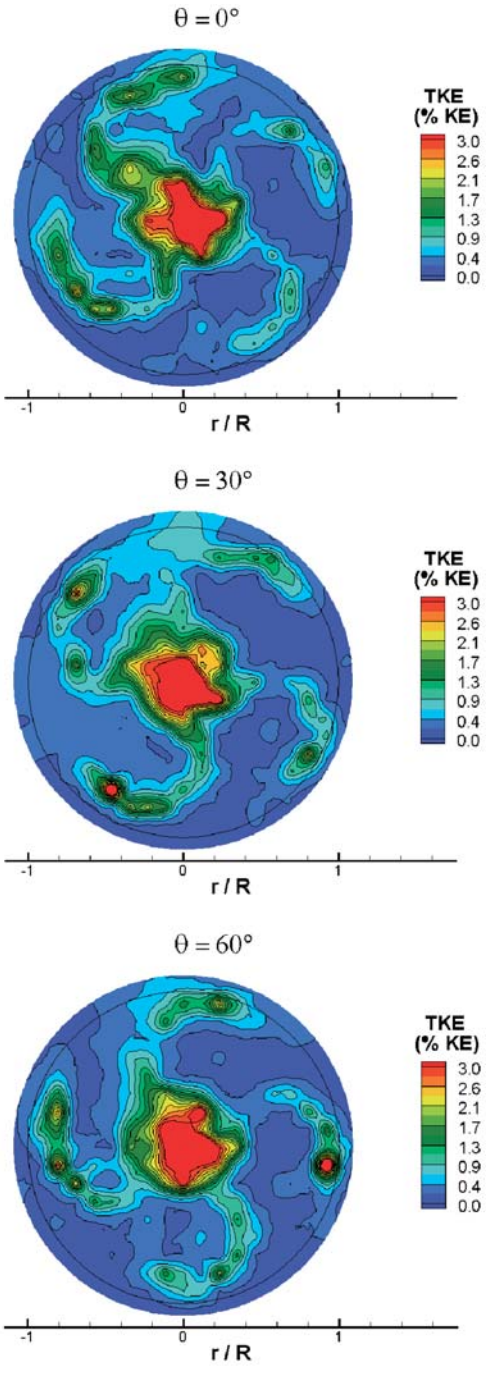

Fig. 19. Downstream wake (x/R = 0.742) with the propeller installed. TKE as a percentage of the free-stream kinetic energy at 0°, 30°, and 60°

dard deviation of the velocity field. As shown in Fig. 19, a weak trace from the shaft and the vertical bracket is still apparent in the turbulent field.

The distribution of the turbulence levels shows the trace of the blade wake in the measurement plane, and also points out the wake deformation due to the tip and hub vortex action. High turbulence levels are observed in the tip vortex core, especially within the brackets area crossing, where a complex interaction between the tip vortex and the wake of the brackets takes place. This strong interaction causes a turbulence diffusion in a wide area due to the tip vortex deformation, stretching,

and random displacement caused by the turbulent wake of the brackets.

An absence of continuity between the trace of the blade's turbulent wake and the tip vortex agrees with similar results found in the literature that point out the viscous nature of the roll-up.[1,2,13]

The interaction between blade turbulence and the shaft wake induces a diffusion of the turbulence in a large region in the upper part of the measurement disc. The convection effect, due to the velocity induced by the propeller, rotates this zone in the sense of the rotation of the propeller.

Propeller-induced acceleration promotes a decrease in the turbulent energy as a consequence of the positive gradient of the axial velocity in the flow direction[15] ($\partial U/\partial x > 0$). This is clear when comparing the contour levels in Figs. 15 and 19: moving from the upstream to the downstream propeller plane, the TKE between the blades is reduced from light blue (Fig. 15) to dark blue (Fig. 19).

To complete the description of the velocity field in the propeller wake, Fig. 20 shows the cross-flow in the downstream plane for the angles $\theta = 0°$, 30°, and 60°. The vector field indicates the swirling effect induced by the hub vortex and the roll-up around the cores of the tip vortices, which are stronger in the inner half of the measurement plane than elsewhere.

Figure 21 represents the distribution of the x-component of the vorticity, calculated from the cross-flow components V_y and V_z as

$$\omega_x = \frac{\partial V_z}{\partial y} - \frac{\partial V_y}{\partial z} \tag{5}$$

The vorticity field allows us to investigate the complex nature of the hub vortex and the trace of the trailing vortex sheet shed from the struts and the blades as a consequence of the radial gradient of the bound circulation $\Gamma(r)$. The vorticity distribution along the span of the blade changes the sign at approximately $r/R = 0.65$, where the blade achieves the maximum circulation and load. The unsteadiness of the blade's hydrodynamic load is responsible for a secondary structure shedding near the tip vortex, whose intensity and direction change as a consequence of the modulation of the circulation with the variable loading condition.

The shape and intensity of the vortical trace released by the blades change during the revolutions as a consequence of the different loading conditions. The strong modification of the wake's shape stresses the importance of considering the angular variation of the propeller inflow, which is often ignored in CFD calculations in order to reduce the computational costs, and instead the nominal wake is integrated along the circumference at a given radius.

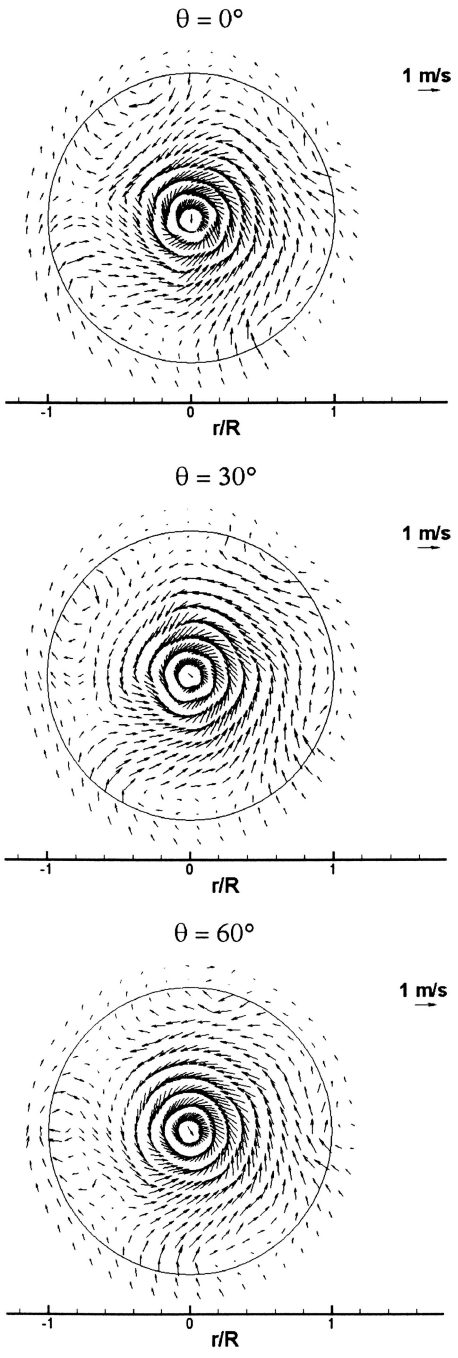

Fig. 20. Downstream wake ($x/R = 0.742$) with the propeller installed. Vector field at 0°, 30°, and 60°

6.5 Blade hydrodynamic load analysis based on the effective wake

Information on the effective blade loading conditions can be achieved by analysing the downstream wake results. This approach considers the tip vortex circulation $\Gamma(\vartheta)$, which is estimated on the basis of the vorticity flux over the tip vortex trace for each position of the reference blade:

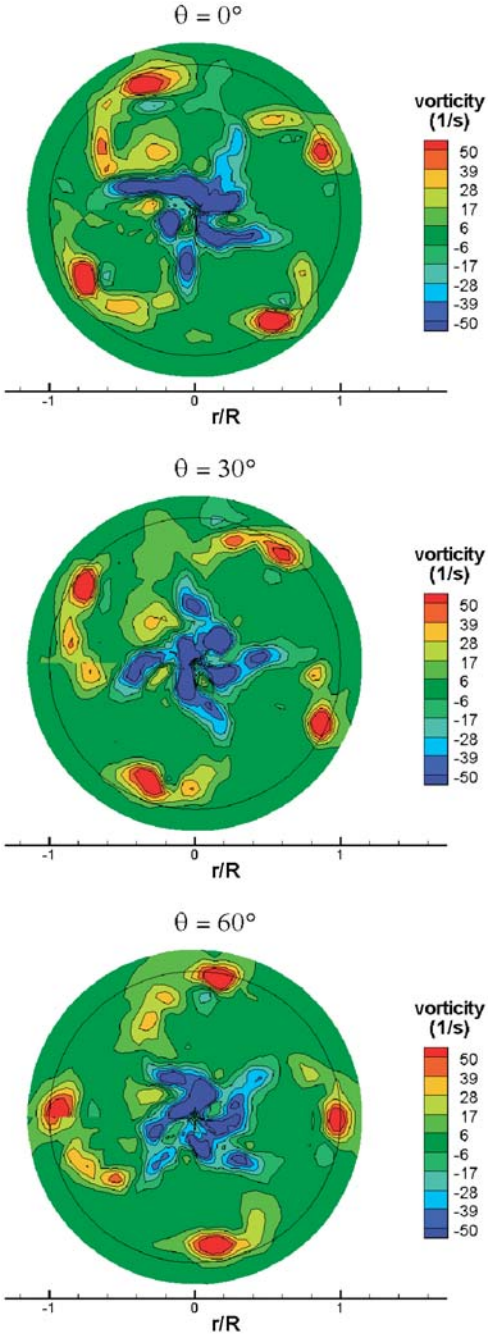

Fig. 21. Downstream wake (x/R = 0.742) with the propeller installed. Vorticity field at 0°, 30°, and 60°

$$\Gamma(\vartheta) = \iint_{\text{tip vortex}} \overline{\omega} \cdot \overline{n} \, \mathrm{d}S \tag{6}$$

The angular evolution of the circulation of the tip vortex and the blade load index are plotted in Fig. 22. A qualitative comparison between these diagrams allows us to point out the effect of the nonuniformity of the inflow from two different points of view: nominal wake

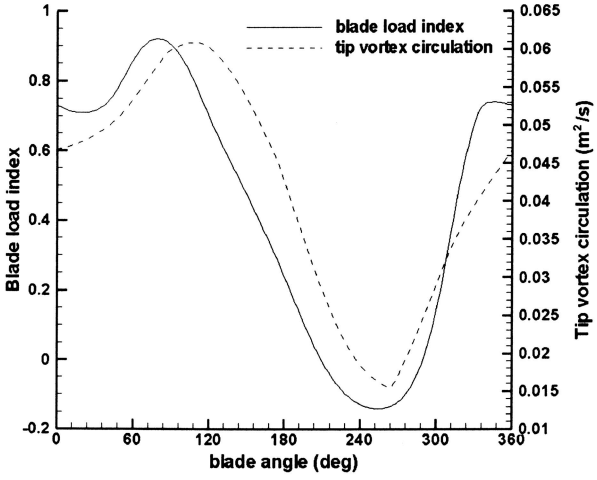

Fig. 22. Comparison between the evolution of the circulation of the tip vortex and the blade load index

(blade element theory and downstream wake) and tip vortex circulation. This comparison shown a substantial agreement with a phase difference consequence of the wake swirl between the propeller disc and the downstream plane.

7 Conclusions

The LDV phase sampling technique adopted allows an effective reconstruction of an installed propeller wake. The experimental results show significant features of the flow field around an installed propeller.

— In the upstream wake, the propeller effect is apparent as a four-lobe structure, representing the velocity peaks induced by the blades, which rotates in phase with the positions of the blades. The turbulent field appears to be very similar to the nominal wake field: the propeller-induced acceleration leads to a slightly narrower trace from the wakes of the brackets and the shaft, and a global reduction of turbulence levels.
— The downstream wake loses the axisymmetric morphology which is typical of a propeller wake in uniform inflow, with a centroid thrust displacement toward the inner half of the measurement plane (for the propeller revolution configuration adopted), where the hydrodynamic load is larger.
— The nominal wake gives a good qualitative estimation of the hydrodynamic load of the blade. This is confirmed by the good agreement with the evolution of the circulation of the tip vortex, calculated from the downstream wake.
— The turbulent wake of the brackets and shaft destabilizes the propeller tip vortex system; this is high-

lighted by the increased turbulence levels of the core of the tip vortex when crossing this region.
— The effect of the unsteadiness of the propeller load causes a secondary structure shedding near the tip vortex, whose intensity and direction change due to the modulation of the circulation to the variable loading conditions.

Acknowledgments. This work was supported by the Ministero delle Infrastrutture in the frame of the INSEAN Research Program 2000–2003. The authors thank Dr. F. Salvatore for his useful comments and suggestions.

References

1. Kobayashi S (1982) Propeller wake survey by laser–Doppler velocimeter. In: Proceedings of the 4th international symposium on application of laser anemometry to fluid mechanics, Lisbon
2. Jessup S (1976) An experimental investigation of viscous aspects of propeller blade flow. MIT Department of Ocean Engineering, 76–6
3. George WK, Lumley JL (1973) The laser–Doppler velocimeter and its applications to the measurement of turbulence. J Fluid Mech 60:321–362
4. Min KS (1978) Numerical and experimental methods for the prediction of field point velocities around propeller blades. MIT Department of Ocean Engineering, 78–12
5. Hoshino T, Oshima A (1987) Measurement of the flow field around a propeller by using a 3-component laser–Doppler velocimeter. Mitsubishi Technical Review, No. 24
6. Chesnakas C, Jessup J (1998) Experimental characterisation of propeller tip flow. In: Proceedings of the 22nd symposium on naval hydrodynamics, Washington, DC
7. Cenedese A, Accardo L, Milone R (1988) Phase sampling in the analysis of a propeller wake. Exp Fluids 6:55–60
8. Lammers G (1982) LDA measurements of the tip vortex velocity field in the slipstream of marine propellers. In: Proceedings of the 4th international symposium on application of laser anemometry to fluid mechanics, Lisbon
9. Stella A, Guj G, Di Felice F (2000) Propeller flow field analysis by means of LDV phase sampling techniques. Exp Fluids 28:1–10
10. Hyun BS, Patel VC (1991) Measurements in the flow around a marine propeller at the stern of an axisymmetric body. Exp Fluids 11:33–44
11. Rood EP, Anthony DG (1988) An experimental investigation of propeller hull appendage hydrodynamic interaction. In: Proceedings of the 17th symposium on naval hydrodynamics, Hague
12. Di Felice F, Felli M, Ingenito G (2000), Propeller wake analysis in nonuniform inflow by LDV. In: Proceedings of the propeller shafting symposium, Virginia Beach, USA
13. Stella A, Guj G, Di Felice F, et al (2000) Experimental investigation of propeller wake downstream evolution by means of LDV and flow visualizations. J Ship Res 44:159–173
14. Di Felice F, Di Florio D, Felli M, et al (2004) Experimental investigation of the propeller wake at different loading conditions by particle image velocimetry. J Ship Res 48:168–190
15. Hinze JO (1975) Turbulence. McGraw Hill, New York